Toroidal Alfvén eigenmodes observed in low power JET deuterium-tritium plasmas

H. J. C. Oliver[1], S. E. Sharapov[1], Ž. Štancar[1], M. Fitzgerald[1], E. Tholerus[1], B. N. Breizman[2], M. Dreval[3], J. Ferreira[4], A. Figueiredo[4], J. Garcia[5], N. Hawkes[1], D. L. Keeling[1], P. G. Puglia[6,1], P. Rodrigues[4], R. A. Tinguely[7], and JET contributors[*]

[1]United Kingdom Atomic Energy Authority, Culham Science Centre, Abingdon, Oxon, OX14 3DB, UK
[2]Institute for Fusion Studies, University of Texas at Austin, Austin, Texas 78712, USA
[3]National Science Centre, Kharkiv Institute of Physics and Technology, 61108 Kharkiv, Ukraine
[4]Instituto de Plasmas e Fusão Nuclear, Instituto Superior Técnico, Universidade de Lisboa, Portugal
[5]CEA, IRFM, 13108 Saint-Paul-Lez-Durance, France
[6]Ecole Polytechnique Fédérale de Lausanne, Swiss Plasma Center, CH-1015 Lausanne, Switzerland
[7]Plasma Science and Fusion Center, Massachusetts Institute of Technology, Cambridge, Massachusetts 02139, USA

[*]See the author list of 'Overview of JET results for optimising ITER operation' by J. Mailloux et al 2022 Nucl. Fusion 62 042026

Abstract

The Joint European Torus (JET) recently carried out an experimental campaign using a plasma consisting of both deuterium (D) and tritium (T). We observed a high-frequency mode using a reflectometer and an interferometer in a D-T plasma heated with low power neutral beam injection, $P_{NBI} = 11.6\ MW$. This mode was observed at a frequency $f = 156\ kHz$ and was located at major radii $3.1 \leq R(m) \leq 3.3$. The observed mode was identified as a toroidal Alfvén eigenmode (TAE) using the linear MHD code, MISHKA. Beam ions and fusion-born alpha particles were modelled using the full orbit particle tracking code LOCUST, which produces smooth distribution functions suitable for stability calculations without analytical fits or the use of moments. We calculated the stability of the 21 candidate modes using the HALO code. These calculations revealed that beam ions can drive TAEs with toroidal mode numbers $n \geq 8$ with linear growth rates $\gamma_b/\omega \sim 1\%$, while TAEs with $n < 8$ are damped by the beam ion population. Alpha particles drive modes with significantly smaller linear growth rates, $\gamma_\alpha/\omega \lesssim 0.1\%$ due to the low alpha power generated almost exclusively by beam-thermal fusion reactions. Non-ideal effects were calculated using complex resistivity in the CASTOR code, leading to an assessment of radiative, collisional, and continuum damping for all 21 candidate modes. Ion Landau damping was modelled using Maxwellian distribution functions for bulk D and T ions in HALO. Radiative damping, the dominant bulk damping mechanism, suppresses modes with high toroidal mode numbers. Comparing the drive from energetic particles with damping from thermal particles, we find all but one of the candidate modes are damped. The single net-driven $n = 9$ TAE with a net growth rate $\gamma_{net}/\omega = 0.02\%$ matches experimental observations with a lab frequency $f = 163\ kHz$ and location $R = 3.3\ m$. The TAE was driven by co-passing particles through the $v_\parallel = v_A/5$ resonance. Both co- and counter-passing alpha particles drive the TAE through the $v_\parallel = v_A/3$ resonance. Additional sideband resonances contribute significant drive for both beam and alpha particles.

1 Introduction

Toroidal Alfvén eigenmodes (TAEs) [1] are weakly damped modes of plasma oscillation that can be excited by populations of fast ions in tokamak plasmas. TAEs have been studied extensively due to their

ability to transport energetic particles. Redistribution of fast ions degrades fusion reactor performance and can potentially damage the first wall of a tokamak if sufficient numbers of energetic particles are moved onto unconfined orbits during the interaction with the TAE. The amplitude of a TAE resonating with a population of energetic particles will evolve with the linear growth rate,

$$\frac{\gamma}{\omega} \propto \omega \frac{\partial f}{\partial E} + n \frac{\partial f}{\partial P_\phi}, \tag{1}$$

where n is the toroidal mode number, ω is the eigenfrequency, and $f(\sigma, E, \mu, P_\phi)$ is the energetic particle distribution function. The distribution function depends on the direction of parallel motion relative to the plasma current $\sigma = sign(v_\parallel)$, the particle energy E, the magnetic moment μ, and the canonical toroidal angular momentum $P_\phi = m_j R v_\phi + e_j \Psi$, which depends on the particle mass m_j, charge e_j, major radius R, toroidal velocity v_ϕ, and poloidal flux Ψ. We have neglected the free energy source associated with gradients in the magnetic moment, which can only drive waves with frequencies close to or above the ion cyclotron frequency ω_{ci}. Equation 1 is often rewritten in terms of the ion diamagnetic frequency [2]:

$$\omega_* = \frac{\partial f}{\partial P_\phi} \Big/ \frac{\partial f}{\partial E} \tag{2}$$

to obtain the condition for instability: $n\omega_* > \omega$. This energy can be readily accessed if the wave resonates with energetic particles with bounce-averaged toroidal and poloidal frequencies of motion, $\langle \dot{\phi} \rangle$ and ω_b, which satisfy the resonance condition [2]:

$$\omega + n\langle \dot{\phi} \rangle + p\omega_b = 0, \tag{3}$$

where p is an integer that describes each Fourier component of the power transfer. For passing particles resonating with TAEs, the resonance condition can be written in terms of the parallel velocity $v_\parallel = v_A/|2(m+p)+1|$, where m is the poloidal mode number. Energetic ions are introduced by auxiliary heating schemes, such as neutral beam injection (NBI) and ion cyclotron resonance heating (ICRH). In plasmas composed of deuterium and tritium, appreciable numbers of fusion-born alpha particles may also be present.

The stability of Alfvén eigenmodes (AEs) due to interactions with fast particles is routinely calculated numerically using approximate representations of the fast particle distribution function. These approximations remove spurious gradients introduced by noise, and therefore erroneous drive or damping, by reducing the fidelity of the model. The simplest approach uses analytical expressions for the fast particle distribution function. The energy and spatial distribution can be assumed to follow the slowing down distribution function [3, 4]. The dependence on pitch angle $\lambda = v_\parallel/v$ or the pitch invariant $\Lambda = \mu B_0/E$ is either neglected by assuming isotropy or approximated with a simple analytical expression. These functions are combined by assuming the variables are independent and the distribution function is separable. More physics can be added by using analytical fits or moments of distribution functions generated by Monte Carlo codes, which follow the motion of the full orbit or guiding centre orbit of fast particles in a tokamak. Fits of the Monte Carlo generated distribution function itself (e.g. [5]) retain finite orbit and anisotropic effects. However, this method smooths over important features of the distribution function to mitigate the impact of noise on the stability calculation [6].

In this study, we exploit the full capability of a Monte Carlo code by retaining the resultant distribution function without fitting the distribution function or using moments in the stability calculation. This technique was previously unreliable due to statistical noise, but the use of GPU hardware enables the calculation of high-resolution, smooth distribution functions required for stability calculations. Thereby, we retain critical features of the distribution function that are usually lost in the fitting process, including

the trapped-passing boundary, the full, half and third energy injection of the beam, the magnetic axis, the $v \geq v_{\perp}$ boundary, and the complex inter-dependencies of the constants of motion. We used the Monte Carlo code LOCUST [7] to generate high-resolution, smooth distribution functions. These distribution functions were used in the HALO code [8], which models wave-particle interactions, to assess the stability of several candidate modes. Thereby, we identified a single net-driven TAE that matched experimental observations from our D-T experiment. This new technique revealed the conditions required for modes to be driven unstable by beam ions, which were previously considered to heavily damp TAEs in JET [9, 10, 11], through ion Landau damping.

2 Experimental observations

We designed an experiment to generate a bump-on-tail energy distribution in the alpha particle population. Positive gradients in energy were produced by modulating the beam power on timescales shorter than the alpha particle slowing down time. The experiment aimed to excite Alfvén eigenmodes with these positive energy gradients (through the first term in Equation 1). ICRH was absent to remove any ambiguity around the source of drive for observed modes. However, modes were observed before the beam modulation began. In this paper, we focus on modes excited at time $t = 7.55\ s$ in JET pulse #99503. A discussion of other experimental results can be found in Reference [12].

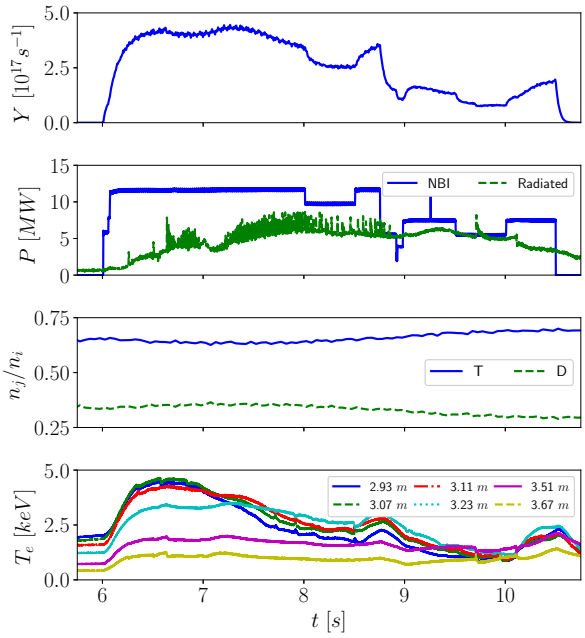

Figure 1: The time evolution of the fusion yield Y; power P of NBI and radiation; the concentrations of ions $j = D, T$ relative to the ion density n_i; and the electron temperature T_e calculated at various major radii for shot #99503.

Throughout the pulse, the equilibrium magnetic field $B_0 = 3.7\ T$ and the plasma current $I_p = 2.5\ MA$. The time evolution of important plasma parameters is depicted in Figure 1. At the time of interest, the fusion yield reaches $4.22 \times 10^{17}\ s^{-1}$ (first frame), near the peak value of $4.45 \times 10^{17}\ s^{-1}$. The fusion yield was dominated by beam-thermal fusion reactions, which are strongly dependent on the deuterium beam power (second frame), $P_{NBI}(t = 7.55s) = 11.6MW$, and the D/T mix of the plasma (third

frame), $D : T(t = 7.55s) = 35\% : 63\%$ with the rest of the ion mix composed of Beryllium, Tungsten and Nickel impurities. The reaction rate was modest for a D-T experiment due to the low beam power, producing $1.19\ MW$ of fusion power, or $240\ kW$ of alpha power, corresponding to a fusion gain of $Q = 0.1$. Beam ions were injected with a maximum energy of 115 keV, although most beam ions are injected at either half or one third of the full energy. The ratio between full, half and third energy beam injection is $33\% : 42\% : 25\%$.

The presence of edge localised modes (ELMs) in the radiated power signal (second frame of Figure 1) shows the plasma in H-mode at the time of interest. Approximately half of the beam power was radiated away, due to impurity accumulation exacerbated by the absence of ICRH. The high radiation causes the electron temperature in the core to become hollow for major radii $2.91 < R[m] < 3.17$, which is visible in the final frame of Figure 1.

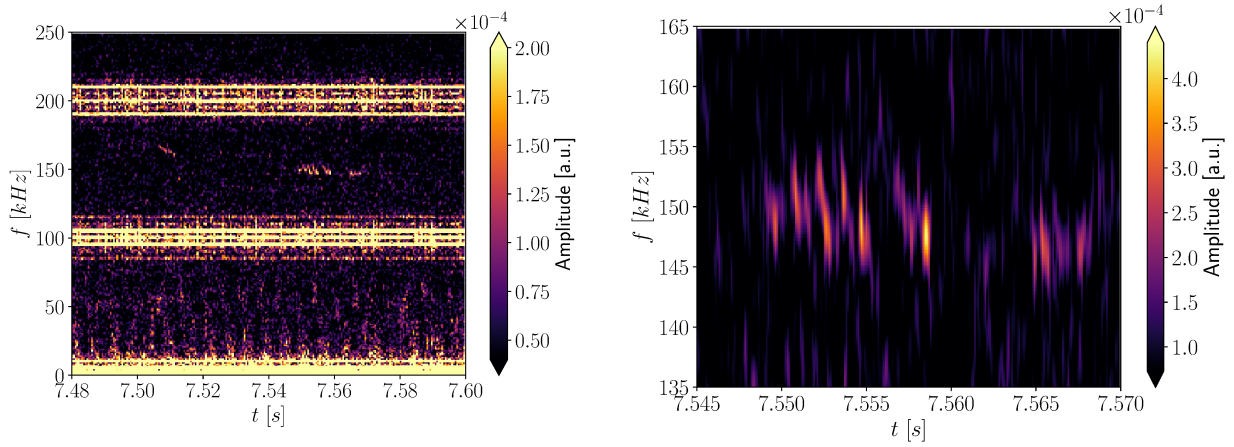

Figure 2: Spectrograph of the perturbed density measured by the fast far-infrared interferometer for shot #99503. The modes of interest are observed at $f = 156\ kHz$ at time $t = 7.55\ s$. They are chirping in frequency, as the zoom on the right shows. The horizontal lines around $f = 0, 100, 200\ kHz$ are artefacts from the diagnostic.

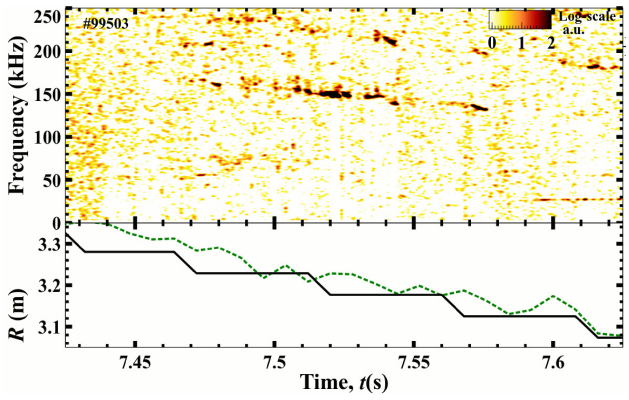

Figure 3: The spectrograph of the reflectometer signal (top) for shot #99503, which depends on the radial localisation of the reflectometer cut-off position calculated using two different estimates of plasma density to calculate the cut-off position (bottom).

Figure 2 shows the spectrograph of the density perturbation measured by a fast far-infrared interferometer [13]. A mode can be observed at a frequency $f = 156\ kHz$ at time $t = 7.55\ s$. A closer inspection of the modes observed in the interferometer signal reveals chirping behaviour, with the mode frequency sweeping down from $156\ kHz$ to $144\ kHz$. Weaker modes are also observed at $t = 7.50\ s$ and $f \approx 170$ kHz. The frequency of the modes observed at $7.55\ s$ is lower than the modes at $7.50\ s$ because the q profile is increasing with time.

The modes were also observed using an X-mode correlation reflectometer [14], as Figure 3 demonstrates. The probing beam of the reflectometer was programmed to sweep down in frequency and hence cut-off location [15] with a period of 0.6 s, allowing the reflectometer to probe the perturbed density at different radial positions $2.7 \lesssim R(m) \lesssim 3.7$. Therefore, any observed modes can be radially localised within error bars of $\pm 0.1\ m$. The signal is an amalgamation of information about the time of mode excitation and the position of the excited mode. A clear signal was observed at $135 \lesssim f(kHz) \lesssim 170$ at a major radius $3.1 \lesssim R(m) \lesssim 3.3$ with error bars of $\pm 0.1\ m$. There were also distinct signals at higher frequencies, but these were not observed in other diagnostics so were not investigated further.

The modes were not observed on magnetic pick-up coils located at the plasma edge. The magnetic coils are more sensitive to modes located near the plasma edge, which undergo less screening by the plasma. The reflectometer indicates that the observed mode was located deep in the plasma so the perturbed magnetic field was likely to be screened by the plasma. Additionally, the modes were relatively weak signals, which may decay to unobservable levels near the magnetic coils. The lack of data from multiple magnetic coils makes it impossible to determine the toroidal mode numbers of the modes. This makes it considerably harder to identify the mode as we must now consider all likely toroidal mode numbers.

3 Modelling

The equilibrium for shot #99503 at time $t = 7.55\ s$ was reconstructed using the equilibrium code EFIT [16]. The safety factor, shown in Figure 4, increases monotonically from $q = 1.6$ on the magnetic axis. The accuracy of the equilibrium reconstruction was improved using pressure and polarimetry constraints. MHD spectroscopy can be used to assess the accuracy of the q profile by comparison with low frequency MHD modes which attached to known rational surfaces. No low-frequency MHD activity was present at $t = 7.55\ s$, but a weak tearing mode was observed from $8.0\ s$ on several toroidally-separated magnetic coils, enabling the identification of the $m/n = 2/1$ tearing mode. The frequency of this tearing mode, $f_{2/1} = 5.2\ kHz$, can be used to determine the location of $q = 2$ flux surface using the monotonically decreasing rotation frequency profile obtained from charge exchange measurements: $f_{2/1} = n f_{rot}(q = 2)$. This method suggests the tearing mode was located at a major radius $R(q = 2) \approx 3.5\ m$. Additionally, a $3/2$ tearing mode excited at $f_{3/2} = 8.4\ kHz$ from $8.48 \leq t(s) \leq 8.58$ was strong enough to appear on the electron cyclotron emission (ECE) diagnostics, enabling the marker to be accurately located from the position of the ECE line of sight: $R(q = 3/2) \approx 3.2\ m$. Both MHD markers [17] corroborate the accuracy of the q profiles reconstructed with EFIT for this pulse.

Density and temperature profiles are used to compute the collision operators in the LOCUST code. These profiles were calculated using the plasma transport code, TRANSP [18]. The profile reconstruction with TRANSP used electron density measurements from the Thompson scattering and LIDAR diagnostics, electron temperature measurements from Thompson scattering and core ECE diagnostics, and ion temperature and plasma rotation measurements from charge exchange diagnostics. The resultant density and temperature profiles for $t = 7.55\ s$ are shown in Figure 5. The hollow electron temperature profile is clearly visible, as anticipated from the time traces shown in Figure 1. The impurities are

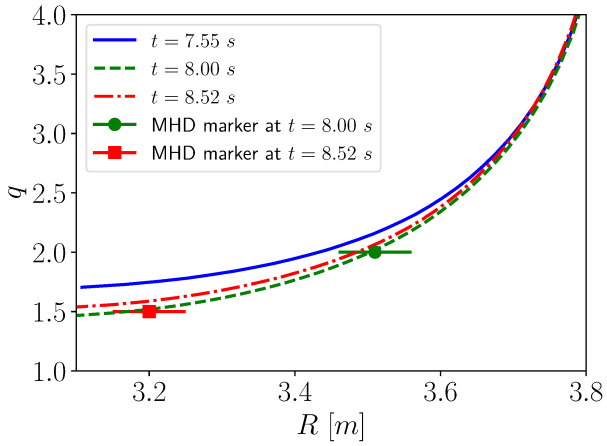

Figure 4: The safety factor q calculated by EFIT as a function of major radius R for shot #99503. Two MHD markers observed later in the pulse are depicted by scatter-points with error bars $\Delta R = 5\ cm$.

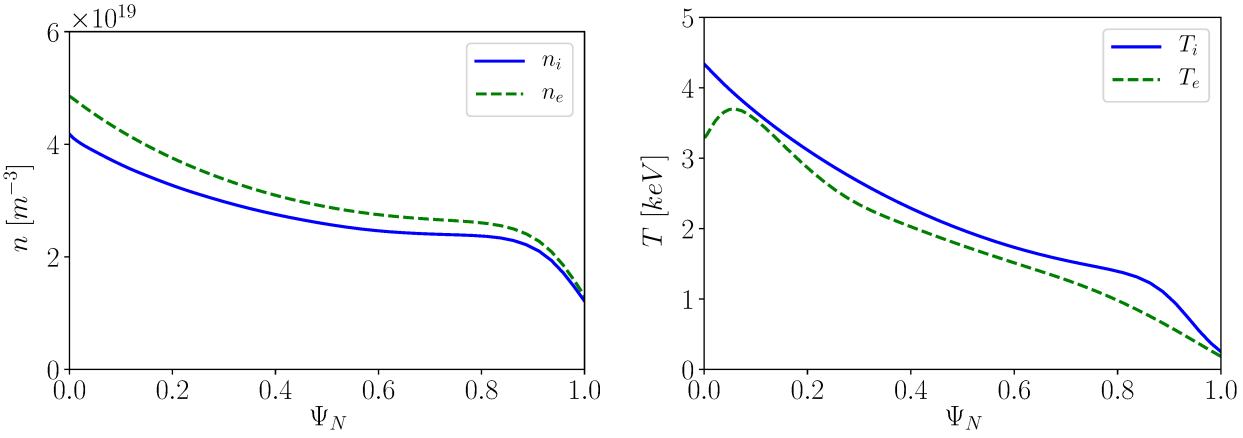

Figure 5: Thermal ion and electron density n and temperature T as a function of normalised poloidal flux Ψ_N reconstructed by TRANSP for shot #99503 at time $t = 7.55\ s$.

modelled in TRANSP as Beryllium and Nickel (representing all mid and high-Z impurities) with relative concentrations $n_{Be}/n_i = 1.13 \times 10^{-2}$ and $n_{Ni}/n_i = 1.80 \times 10^{-4}$. Beryllium impurities are introduced by wall-plasma interactions and Nickel is introduced from impact erosion with the RF antenna.

3.1 Mode identification

The HELENA code [19] was used to convert the EFIT equilibrium into the straight field line coordinates used by the linear MHD codes, CSCAS [20] and MISHKA-1 [21], which solve the ideal, incompressible MHD equations. The shear Alfvén wave continuum was calculated using CSCAS for toroidal mode numbers $0 \leq n \leq 14$, which is plotted for $n = 9$ in Figure 6. 30 poloidal harmonics centred around $nq(R_0)$ are used for each run. From each continuum we identify the upper and lower frequency limits of the TAE gap. MISHKA was then used to obtain all eigenmodes present in the plasma for each toroidal mode number using 20 poloidal harmonics, scanning the initial guess for the eigenfrequency from the lower edge of the TAP gap to the top of the gap over 30 steps. The scanning script automatically saves

unique converged solutions, which were filtered to remove continuum modes. The plasma frequency is obtained by multiplying the eigenfrequency by the Alfvén frequency on the magnetic axis, $\omega_A(0) = v_A(0)/R_0 = 2.50\times10^6\ s^{-1}$. The local toroidal rotation frequency at the location of each candidate mode was added to the plasma frequency of each mode to obtain the mode frequency in the laboratory frame: $f_{lab} = f_{plasma} + nf_{rot}$. We found 80 TAEs that were present in the plasma with toroidal mode numbers $1 \leq n \leq 14$, 25 of which exist in the correct location $0.15 \leq s \leq 0.55$ or $3.0 \leq R(m) \leq 3.4$. Figure 7 shows 21 TAEs with frequencies $120 \leq f(kHz) \leq 180$ that were selected for stability analysis.

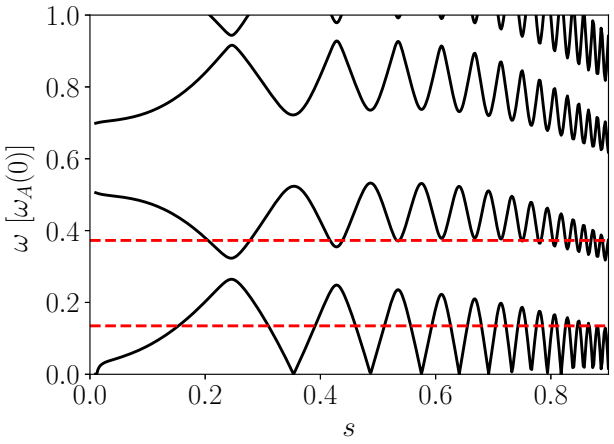

Figure 6: The shear Alfvén wave continuum for the toroidal mode number $n = 9$ at time $t = 7.55\ s$ in shot #99503 showing the frequency ω as a function of the square root of the normalised poloidal flux, $s = \sqrt{\Psi_N}$. The frequency is normalised by the Alfvén frequency on the magnetic axis, $\omega_A(0)$. The red dashed lines denote the frequency limits used for the MISHKA-1 scan.

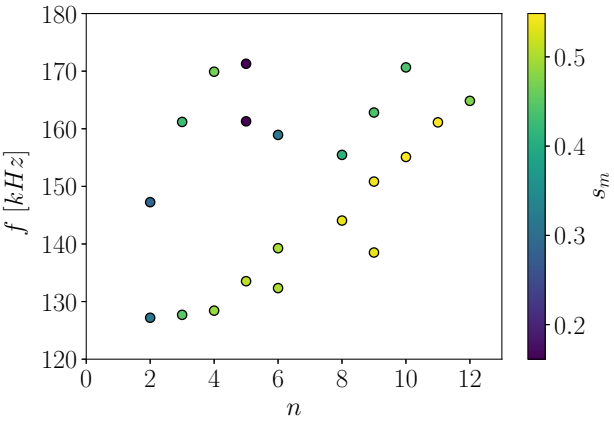

Figure 7: Toroidal Alfvén eigenmodes with toroidal mode number n, frequency f and mode location s_m found using the MISHKA code that match the experimentally observed mode for shot #99503 at time $t = 7.55\ s$.

3.2 Modelling the beam ion distribution function

We calculated the fast particle distribution functions using the LOCUST code [7]. LOCUST follows the full orbit of a sample of fast ions from birth to thermalisation by solving the Lorentz equation of motion

and applying a collision operator. This computationally intensive process is made possible by exploiting the latest GPU hardware. A LOCUST full orbit simulation of $6M$ beam ions spanning $0.5\ s$ of plasma time with a time-step of $2\ ns$ takes 25 hours using four NVIDIA A100 GPU cards. $6M$ beam ions were required to resolve all essential features of the distribution function and obtain good convergence of the linear growth rate in HALO.

The distribution function was calculated by cumulatively binning the fast ion markers on the CPU every $100\ ns$. This process results in the calculation of the steady-state distribution function through sum reduction by using the entire history of one set of markers from birth until thermalisation or loss from the plasma [22].

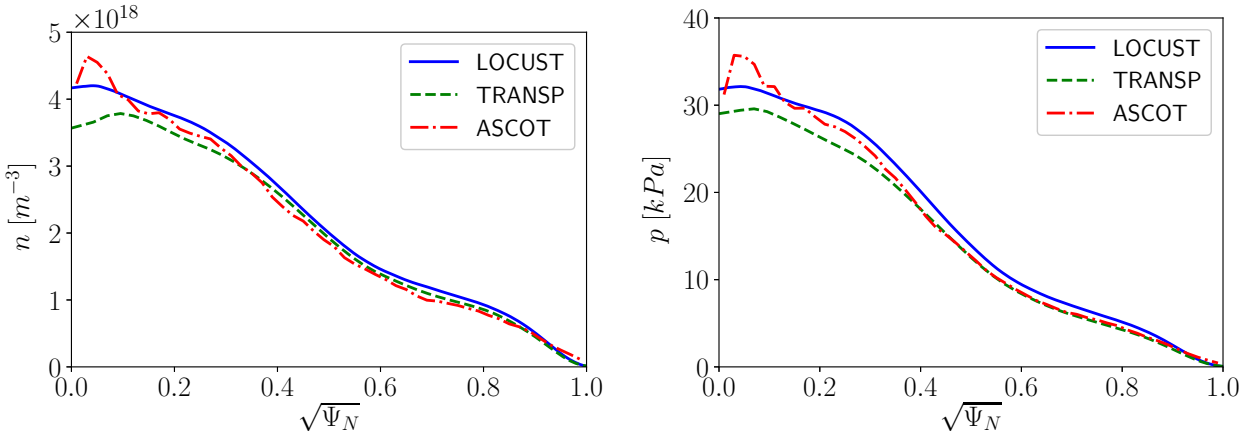

Figure 8: The beam density n and pressure p calculated by LOCUST, ASCOT and TRANSP as a function of the square root of normalised poloidal flux Ψ_N at time $t = 7.55\ s$ in shot #99503.

LOCUST simulations use ion and electron temperature and density profiles from TRANSP, a 3D tetrahedral wall mesh, a `G EQDSK` file describing the equilibrium calculated by EFIT, and a representative sample of markers to follow. The initial sample of beam ions was generated from the beam deposition in TRANSP-NUBEAM [23]. These markers were then followed until thermalisation, or until the particle terminates on a wall tile. Just 0.1 % of beam ions were lost to plasma-facing components. The moments of the distribution function calculated by LOCUST are shown in Figure 8. The result from LOCUST agrees closely with comparable results from two other codes (TRANSP and ASCOT [24]) for both the beam density and pressure. The profiles produced by LOCUST are more smooth than the results from TRANSP and ASCOT due to the high number of markers used in the simulation. The ASCOT run used 20K markers, while the TRANSP calculation used 620K markers.

The co-current beam distribution function calculated by LOCUST is depicted in Figure 9 for various values of the magnetic moment. The distribution function is smooth, which is essential for stability calculations that rely on gradients of the distribution function. The effect of full, half, and third energy injection is preserved and is visible in the top right and bottom frames of Figure 9. The trapped-passing boundary is visible for sufficiently high μ. The left edge in each frame is a result of the condition $\mu B \leq E$, with the angle determined by $B(R)$. The lower edge in each frame corresponds to the magnetic axis, with the angle determined by the first term in the toroidal canonical angular momentum $\sim m_j R v_\phi$. These features are typically lost when using analytical expressions or fits of Monte Carlo-generated distribution functions.

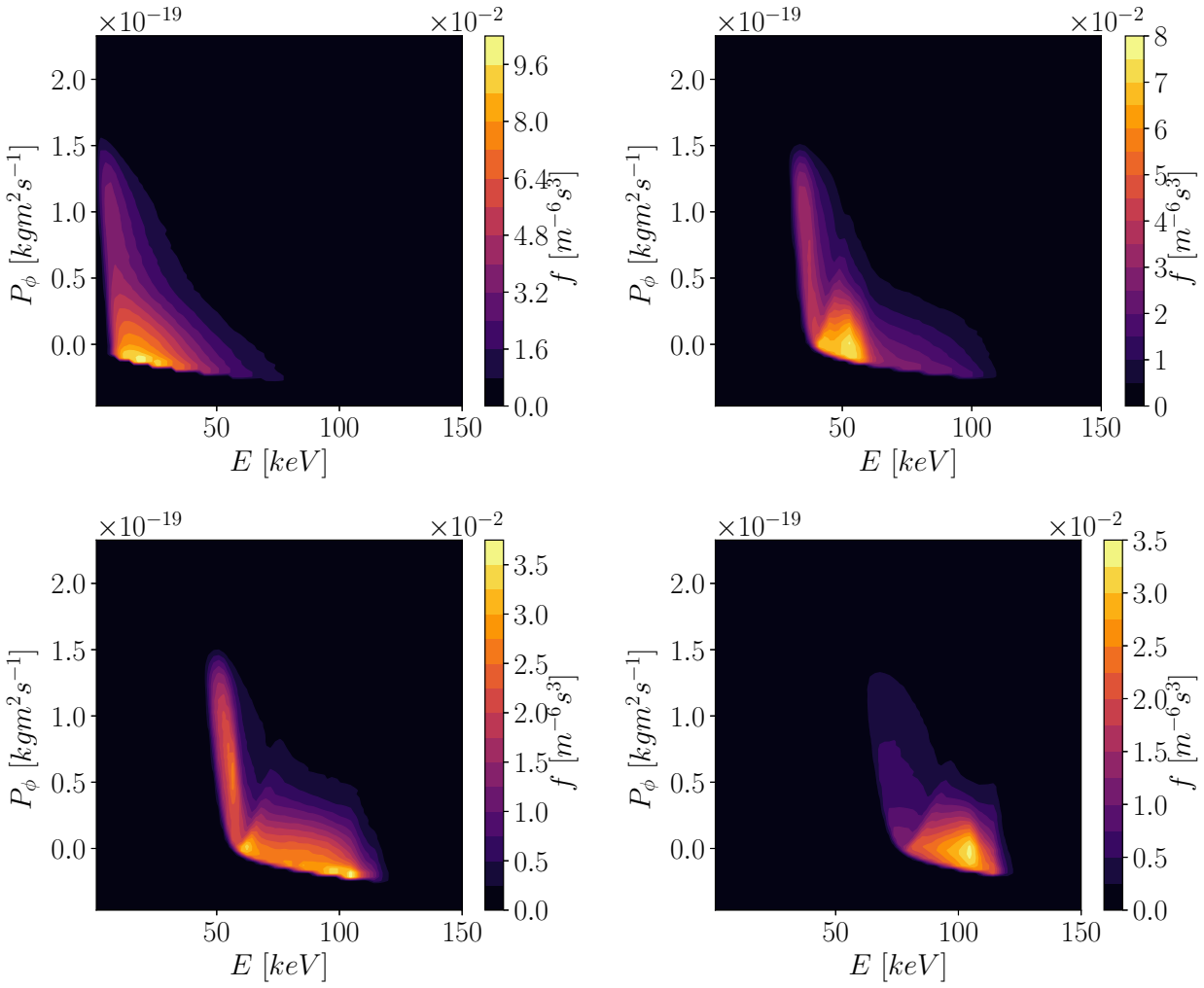

Figure 9: The co-current ($\sigma = +1$) beam distribution function f as a function of energy E and toroidal canonical angular momentum P_ϕ for fixed values of the magnetic moment: $\mu = 1.1keV/T$ (top left), $\mu = 9.6keV/T$ (top right), $\mu = 15.2keV/T$ (bottom left), $\mu = 20.2keV/T$ (bottom right) at time $t = 7.55\ s$ in shot #99503.

3.3 Modelling the alpha particle distribution function

TRANSP simulations show that beam-thermal fusion reactions dominate over thermonuclear and beam-beam reactions for our shot, with 97% of alpha particles produced in beam-thermal reactions. We generate alpha particles born in beam-thermal fusion by using the beam distribution function computed by LOCUST to generate a set of representative beam ions. A set of thermal particles at the same locations as the beam particles was produced from a Maxwellian distribution. The reaction rate for an alpha particle produced in a fusion reaction between each thermal and beam particle was calculated with Bosch-Hale [25] cross-sections and used as the alpha particle weight in LOCUST. The velocity of the alpha particles was determined through the application of kinematic principles to the velocities of the reactants [26].

This sample of alpha particles was followed in LOCUST until thermalisation. The alpha particle distri-

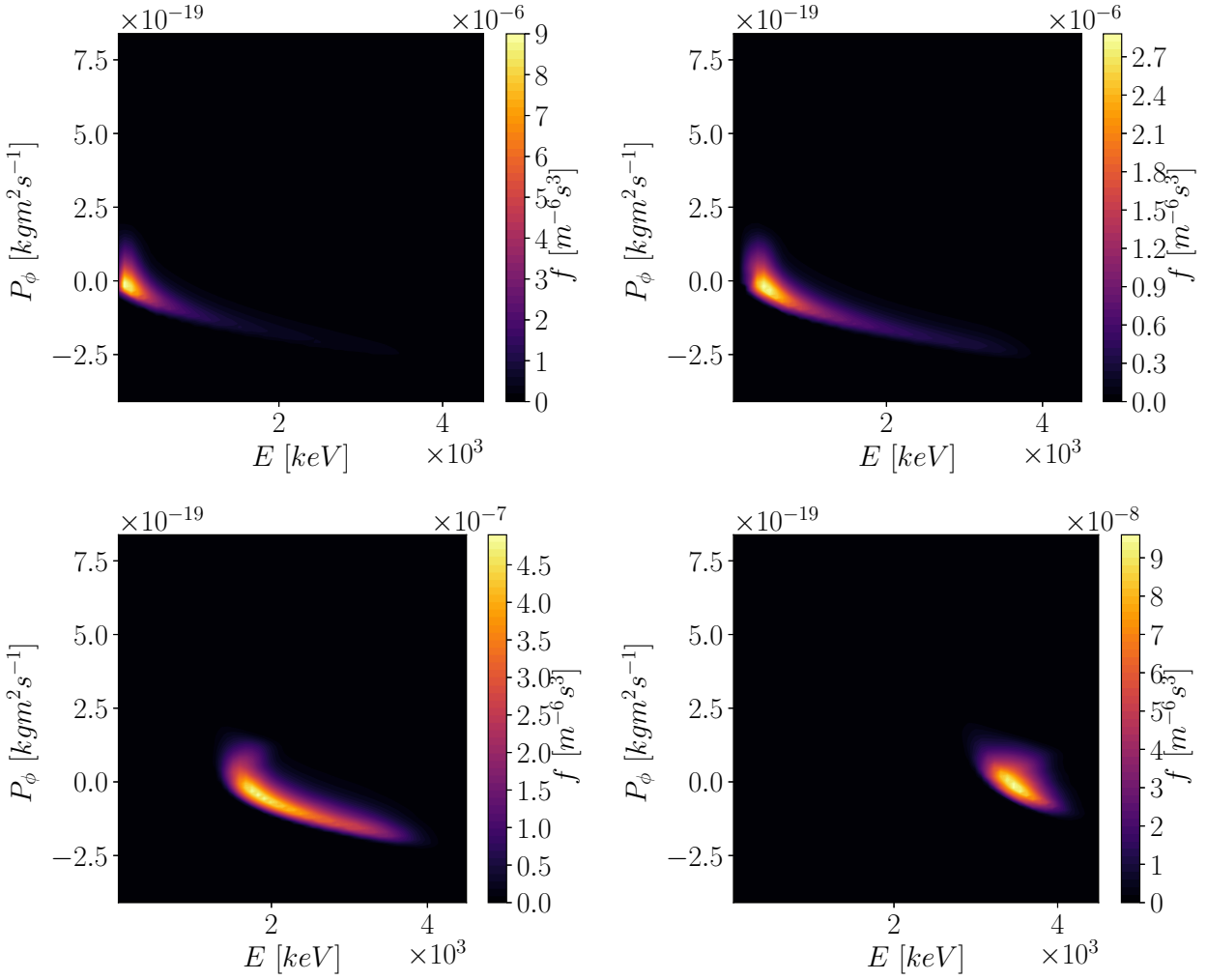

Figure 10: The co-current ($\sigma = +1$) alpha particle distribution function f as a function of energy E and toroidal canonical angular momentum P_ϕ for fixed values of the magnetic moment: $\mu = 43.1keV/T$ (top left), $\mu = 100.5keV/T$ (top right), $\mu = 416.5keV/T$ (bottom left), $\mu = 904.8keV/T$ (bottom right) at time $t = 7.55\ s$ in shot #99503.

bution function is plotted at constant μ in the co-current direction in Figure 10. In general, the alpha particle distribution function is considerably simpler than the beam distribution function. The alpha particle distribution function is strongly peaked around the magnetic axis due to the more narrow birth profile. The distribution function is more peaked in E and P_ϕ at lower μ because the alpha particle orbit width increases significantly with $v_\perp$. The trapped-passing boundary is not as distinct as in the beam distribution function. Due to the relative simplicity of the alpha particle distribution function, using just $1M$ markers in LOCUST was sufficient to capture all of the key features and obtain a converged linear growth rate with HALO.

The moments of the resultant alpha particle distribution function calculated by LOCUST are shown in Figure 11. The density and pressure profiles from LOCUST largely agree with the results from TRANSP and ASCOT. However, the alpha particle density and pressure calculated by LOCUST are slightly lower

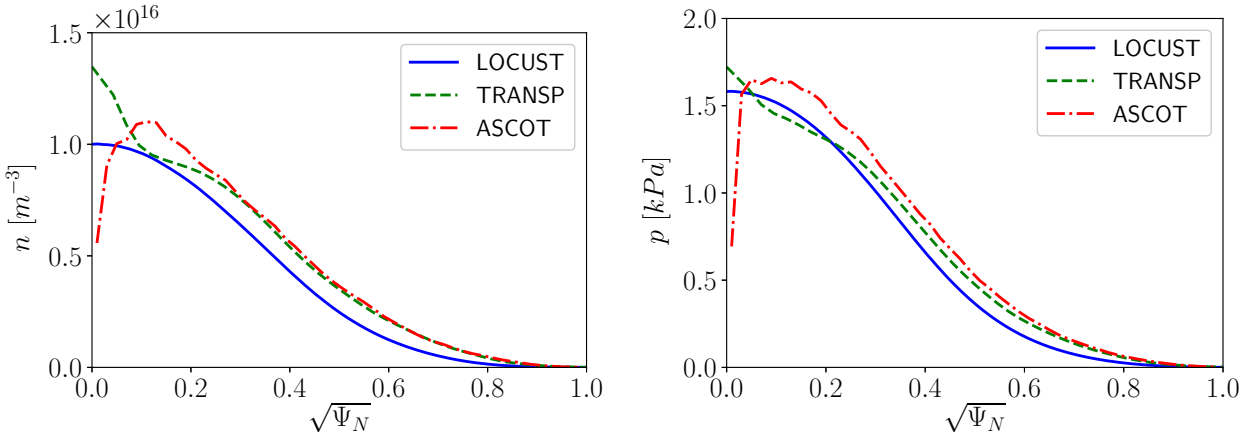

Figure 11: Alpha particle density n and pressure p calculated by LOCUST, ASCOT and TRANSP as a function of the square root of normalised poloidal flux Ψ_N at time $t = 7.55\ s$ in shot #99503.

than the profiles from TRANSP and ASCOT. This difference is due to a higher loss rate of alpha particles calculated by LOCUST, which follows the full gyro-orbit, compared to TRANSP and ASCOT, which follow the particle guiding centres in these simulations. The size of the alpha particle orbits is relatively large compared to the minor radius of the plasma (a), with maximum orbit excursions $\lesssim a/4$. Therefore, a large portion of the fusion-born alpha particles was lost to the plasma-facing components. The gyroradius of alpha particles is large, $\rho_\alpha \lesssim 10\ cm$, finite Larmor radius effects are significant. For $t = 7.55\ s$, 19 % of alpha particles were lost. 95 % of these losses were prompt losses, with collisional scattering onto lost trajectories making up the other 5 % of losses in our axisymmetric equilibrium.

3.4 Modelling the interaction of TAEs with fast particles

The eigenstructure of each candidate mode from MISHKA and the fast particle distribution functions were used as input for the perturbative code HALO [8], which uses a δF scheme [27]. The distribution functions produced by LOCUST require light processing before use in HALO. First, the distribution function must be reshaped to the order used by HALO. Second, singularities present in the $\sigma = -1$ distribution function due to zeroes in the Jacobian were removed using a median filter that replaces each singular point with the local median using three neighbouring points in each dimension.

Full gyro-orbit calculations of linear wave-particle interactions were carried out using the distribution functions calculated with LOCUST and the TAEs found using MISHKA. The stability of each mode shown in Figure 7 was calculated using $4M$ particles that were followed with a time-step of $10^{-10}\ s$. The power transfer with each TAE, which started with initial mode amplitudes $\delta B_r/B_0 = 10^{-7}$, was measured to assess the growth rate of each mode. The power transfer is computed from the work done [8]:

$$P \equiv \int \mathrm{d}\mathbf{x}\delta\mathbf{E} \cdot \delta\mathbf{J}_{\mathbf{fast}}, \tag{4}$$

where $\delta\mathbf{E}$ is the perturbed electric field of the TAE and $\mathbf{J}_{\mathbf{fast}}$ is the fast particle current. The linear growth rate is calculated using the mode energy δW and real wave amplitude a:

$$\gamma = -\frac{P}{a^2 2\delta W}. \tag{5}$$

The stability calculation for each mode required 1.5 hours of computational time using four A100 GPU cards. $4M$ beam markers were required to ensure the fast particle distribution function is accurately represented in HALO and the linear growth rate is converged.

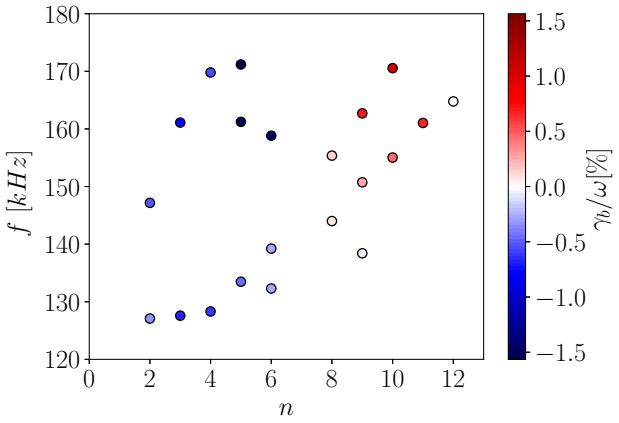

Figure 12: Linear growth rates γ_b normalised to the wave frequency ω due to the interaction of beam ions with 21 TAEs with toroidal mode numbers n and lab frame frequencies f at time $t = 7.55\ s$ in shot #99503.

The linear growth rates due to interactions between the candidate TAEs and the beam ions are shown in Figure 12. The population of beam ions damp TAEs with toroidal mode numbers $n < 8$ with damping rates $-\gamma/\omega \lesssim 1.6\%$. However, TAEs with toroidal mode numbers $n \geq 8$ are driven by P_ϕ gradients in the beam ion distribution function. The mode width $\Delta_m = s_m/m$ is greater than the average orbit width of resonant ions for $n \geq 8$. The drive peaks at $n = 10$ at $\gamma/\omega = 1.0\%$ and begins to slowly decrease for $n \gtrsim 10$ as particle orbits become large relative to the mode width.

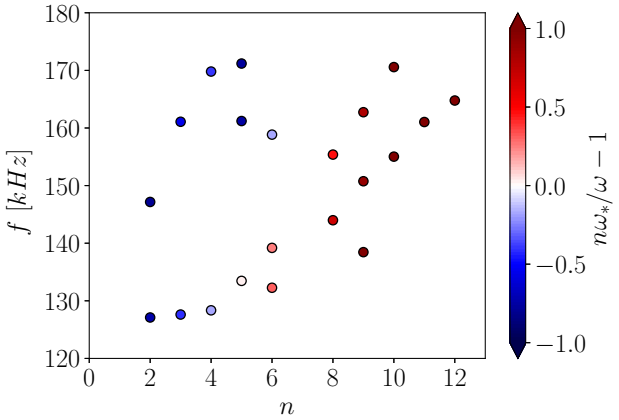

Figure 13: The ion diamagnetic frequency ω_* divided by the wave frequency ω for 21 TAEs at time $t = 7.55\ s$ in shot #99503 with toroidal mode numbers n and lab frame frequencies f. Blue represents damping of a mode, while red signifies drive.

Drive of TAEs by beam ions is unexpected — beam ions are usually assumed to damp TAEs in JET [10, 11]. However, an analytical calculation of the ion diamagnetic frequency $n\omega_*/\omega$ for the slowing down distribution function for the same modes reveals the same qualitative picture: high n TAEs can be driven by radial gradients of the beam pressure, as shown by Figure 13. This is unsurprising when one

considers the first term of Equation 1, which shows that the drive rate from P_ϕ gradients is proportional to the toroidal mode number. As the toroidal mode number increases, the drive from radial gradients can overcome the damping from energy gradients of the distribution function.

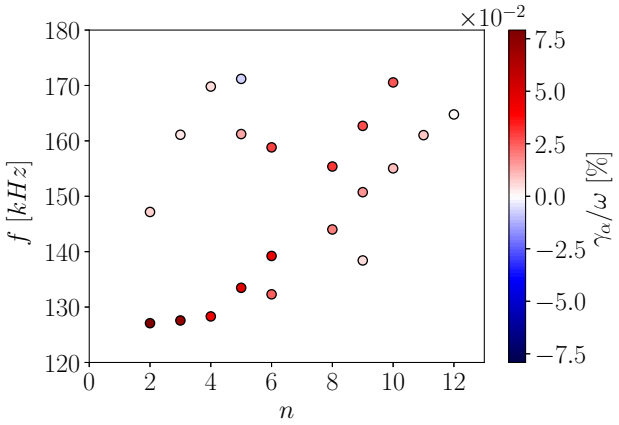

Figure 14: Linear growth rates γ_α normalised to the wave frequency ω due to the interaction of alpha particles with 21 TAEs at time $t = 7.55$ s in shot #99503 with toroidal mode numbers n and lab frame frequencies f.

The resultant linear growth rates are shown in Figure 14. The growth rates due to alpha particles are approximately one of magnitude smaller than those of beam ions due to the low alpha power generated in this experiment. All TAEs except one odd mode were driven by the alpha particle population. The growth rate due to the interaction between alpha particles and the candidate modes was computed using the same method as the beam ion calculation. However, the number of HALO markers required for a converged growth rate is significantly lower for alpha particles than for beam ions due to the simplicity of the distribution function. HALO simulations using $131K$ alpha particle markers compute the linear growth rate to within 10% of the value obtained using $4M$ markers.

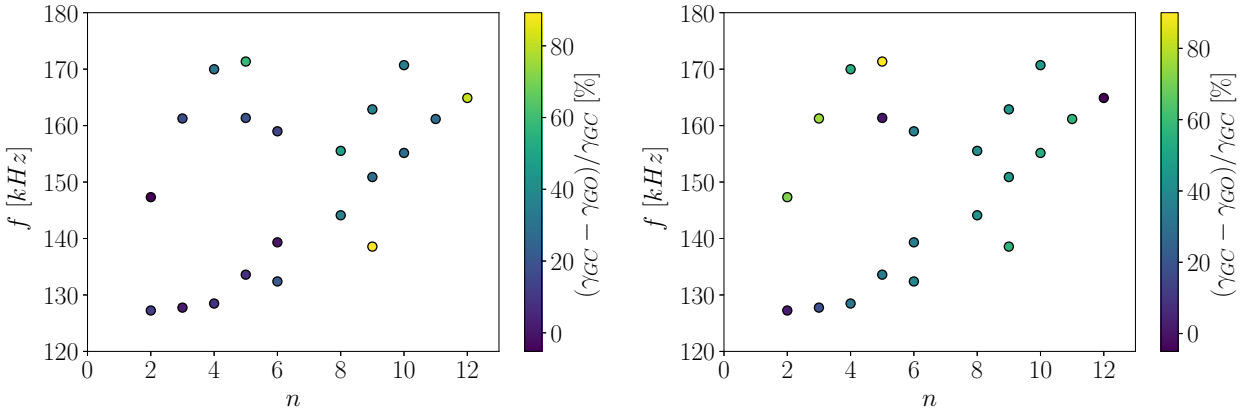

Figure 15: The difference between the guiding centre (GC) and gyro-orbit (GO) calculations of the linear growth rate caused by beam ions (left) and alpha particles (right) for 21 TAEs at time $t = 7.55$ s in shot #99503 with toroidal mode numbers n and lab frame frequencies f.

Guiding centre calculations are approximately 100 times faster than gyro-orbit calculations, but the

time saved comes at the cost of accuracy. The difference between the growth rate from the guiding centre and gyro-orbit calculations increases with toroidal mode number, as depicted in Figure 15. When the mode width is comparable to the fast ion gyroradius, $\Delta_m \sim \rho_f$, the drive of the mode reduces due to a weakening of the resonant particle coupling to the mode. Analytical expressions account for this by including an additional factor $J_0(\rho_f/\Delta_m)$ [28] for full orbit calculations of the linear growth rate compared to guiding centre calculations, where J_0 is the zeroth Bessel function of the first kind. While the difference is greater (and well known) for alpha particle stability calculations, the discrepancy is also significant for calculations of beam ions resonating with TAEs with $n \gtrsim 8$. The discrepancy between gyro-orbit and guiding centre calculations is more significant at low n for alpha particles than for beam ions. TAEs located at higher major radii were also more strongly affected, due to the lower local magnetic field and therefore larger factor $\sim 1/\omega_{ci}$. Figure 15 underlines the importance of using full gyro-orbit calculations for both beam and alpha particles, particularly for high n marginally unstable modes, or modes in weak magnetic fields.

3.5 Computing damping due to interactions with the bulk plasma

The interaction with fast particles is just one aspect of the mode stability. Non-ideal effects, such as parallel electric fields and the finite Larmor radius of thermal particles, couple TAEs with kinetic Alfvén waves (KAWs) [29]. KAWs can propagate perpendicular to the equilibrium magnetic field, carrying energy away from the TAE in the parallel electric field. As the KAW reaches regions with high radial wavenumber (k_r) and thus high dissipation, this energy is transferred to the electron population in a process known as radiative damping. The coupled TAE-KTAE propagates with the dispersion relation [30]:

$$\omega^2 = k_\parallel^2 v_A^2 \left[1 + k_\perp^2 \rho_i^2 \left(\frac{3}{4} + \frac{T_e}{T_i}\left(1 - \mathrm{i}\delta\right)\right)\right], \tag{6}$$

where the thermal ion Larmor radius $\rho_i = \sqrt{m_i T_i}/eB$ and δ represents the dissipation of the energy of the kinetic Alfvén wave through electron collisions.

Including non-ideal effects in the wave equation produces equations analogous to the resistive MHD equations with a complex resistivity if $|\eta k_r^2/\omega| \ll 1$, where the complex resistivity is defined as [30, 31]:

$$\eta = \mathrm{i}\left(\frac{3}{4} + \frac{T_e}{T_i}\left(1 - \mathrm{i}\delta\right)\right)\frac{\omega}{\omega_{A0}}\left(\frac{\omega}{\omega_g}\right)^2\left(\frac{\rho_i}{R_0}\right)^2, \tag{7}$$

where $\omega_g = v_A(R)/2qR$ is the frequency of the TAE gap and $\omega_{A0} = v_A(R_0)/R_0$. The inclusion of complex resistivity in the CASTOR code [30] enables the calculation of the radiative damping rate for a mode. For each mode, the imaginary part of the resistivity was calculated at the mode location and kept fixed while δ, and therefore the real part of the resistivity, was steadily decreased to 0 from 1 [31, 32]. For $\delta \ll 1$, the computed damping rate initially increases rapidly with δ. Above a critical value of δ, the computed damping rate becomes linearly dependent on δ when all KAW wave energy is dissipated. Extrapolating the gradient above the critical point back to $\delta = 0$ reveals the radiative damping rate. The left frame of Figure 16 shows the radiative damping rate for the candidate TAEs. As expected from analytical estimates, the radiative damping rate increases with poloidal mode number m and therefore toroidal mode number n. The damping rate $-\gamma_{rad}/\omega \gtrsim 0.5\%$ for all TAEs with $n \geq 8$.

We can also use CASTOR to calculate the damping rate for trapped electron collisional damping, which occurs due to collisional dissipation of eigenmodes caused by collisions of trapped electrons with ions and passing electrons [33]. The damping rate was computed by using the experimental value of the real resistivity and zero imaginary resistivity at the mode location [34]. We find that collisional damping

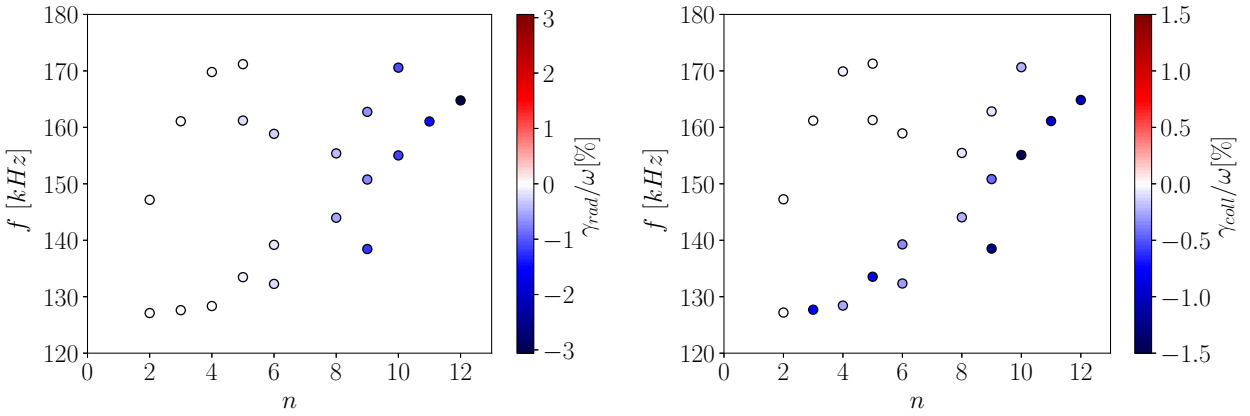

Figure 16: The radiative (left) and collisional (right) damping rates normalised to the wave frequency ω for 21 TAEs at time $t = 7.55\ s$ in shot #99503 with toroidal mode numbers n and lab frame frequencies f.

is most significant for high m even TAEs, as shown by the right frame of Figure 16. The collisional damping rate is sensitive to the mode location, with TAEs at $s_m \geq 0.40$ experiencing more significant collisional damping than TAEs closer to the magnetic axis.

Continuum damping occurs when the eigenfrequency matches the frequency of the shear Alfvén continuum and the mode amplitude is significant at the location of the continuum intersection [35]. This leads to resonant power absorption as the eigenmode is converted into a KAW, which propagates across magnetic field lines and dissipates on the higher density side of the plasma. The continuum damping rate was assessed using CASTOR using only the real part of the resistivity. As the real resistivity tends to zero, the imaginary frequency tends to the continuum damping rate [36, 34]. The continuum damping was small for all TAEs, $2.5 \times 10^{-6} \leq \gamma_{cont}/\omega \leq 1.2 \times 10^{-3}$, due to the small amplitude of the modes at the location at which the eigenfrequency hits the continuum. It was more significant for low n TAEs due to their wide mode width.

Finally, we can use HALO to assess the effect of ion Landau damping, which is caused by the resonant transfer of power from the TAE to thermal ions through relatively inefficient side-band resonances $\sim v_A/v_{Th}/(2j+1)$ where $j \gg 0$. The power transfer can be assessed in HALO using an analytical Maxwellian distribution function instead of the LOCUST-generated distribution function. The linear ion Landau damping rates due to interactions between the bulk D and T ions and the candidate modes were small for all TAEs, $1 \times 10^{-5} \leq \gamma_D/\omega \leq 5 \times 10^{-4}$ and $3 \times 10^{-7} \leq \gamma_T/\omega \leq 1 \times 10^{-3}$, due to the low plasma temperature and high magnetic field of the plasma, which lowers the thermal velocity and increases the Alfvén velocity, respectively.

The dominant bulk damping mechanism was radiative damping, with a significant contribution from collisional damping for even modes at the bottom of the TAE gap. High n even TAEs were heavily bulk damped, while all low n TAEs were heavily damped by beam ions. Comparing the result with the total growth rate due to beam and alpha particles, we find one mode that is marginally unstable, as shown in Figure 17. The net-driven mode with toroidal mode number $n = 9$, lab frequency 163 kHz and location $s_{max} = 0.44$ ($R_{max} = 3.31\ m$) has an even mode structure, as shown in Figure 18, with dominant poloidal harmonics $m = -16$ and $m = -17$ and significant contributions from higher poloidal harmonics. The computed growth rates for the net-driven $n = 9$ mode are shown in Table 1, producing

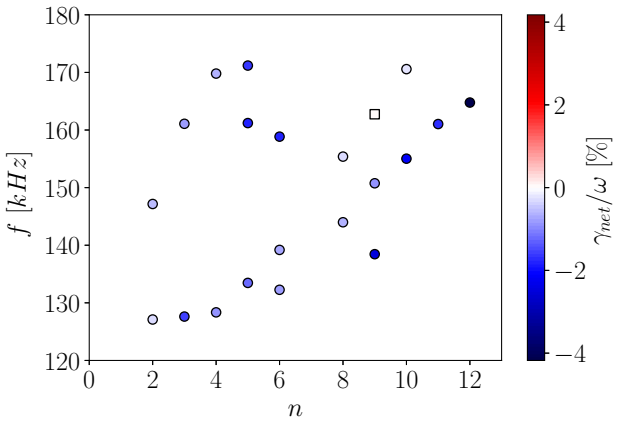

Figure 17: The net growth rate γ_{net} normalised to the wave frequency ω for 21 TAEs at time $t = 7.55$ s in shot #99503 with toroidal mode numbers n and lab frame frequencies f. The single net-driven TAE is marked with a square, while the net damped TAEs are represented by circles.

net drive of $\gamma_{net}/\omega = +0.02\%$. While the drive from alpha particles is small, it plays a key role in pushing the mode from stable to unstable: $\gamma_\alpha > \gamma_{net}$.

γ_b/ω (%)	γ_α/ω (%)	γ_{rad}/ω (%)	γ_{coll}/ω (%)	γ_{cont}/ω (%)	γ_D/ω (%)	γ_T/ω (%)
6.9×10^{-1}	2.8×10^{-2}	-6.0×10^{-1}	-6.7×10^{-2}	-1.5×10^{-3}	-2.7×10^{-3}	-1.0×10^{-3}

Table 1: A table showing the growth rates from beam drive, alpha particle drive, radiative damping, collisional damping, continuum damping, D bulk ion Landau damping and T bulk ion Landau damping for the $n = 9$ net-driven TAE with frequency $f = 163$ kHz at time $t = 7.55$ s in shot #99503.

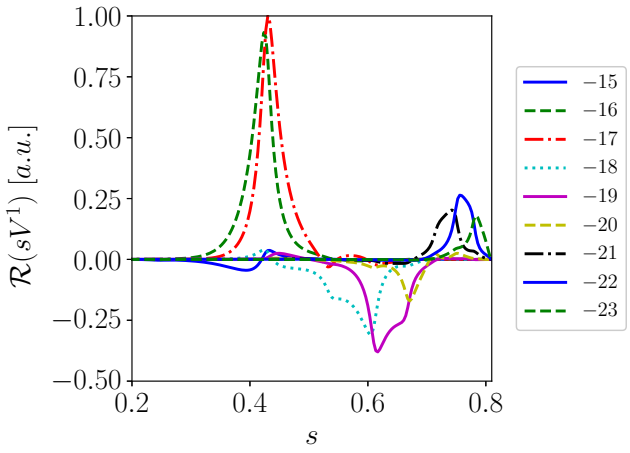

Figure 18: The wave potential $\mathcal{R}(sV^1)$ as a function of the square root of normalised poloidal flux $s = \sqrt{\Psi_N}$ for the net driven $n = 9$ TAE at time $t = 7.55$ s in shot #99503. Different line colours and styles depict significant poloidal harmonics.

3.6 Power transfer between the $n = 9$ TAE and beam ions

The power transfer from each beam ion marker to the $n = 9$ mode is shown in Figure 19. Several distinct resonances with co-passing particles are visible and can be identified by their resonance number p (introduced in Equation 3). The net damping contribution from the $v_{\parallel} = v_A/3$ resonance, which corresponds to a resonance number $p = 15$, is visible at $(\mathcal{E}, \Lambda, P_\phi) = (90keV, 0, 0)$. However, there are few beam ions at such high energies. Instead, higher order resonances play more significant roles in determining the mode stability. The largest contribution to the mode stability comes from the $v_{\parallel} = v_A/5$ ($p = 14$) resonance. The $v_{\parallel} = v_A/5$ resonance damps the TAE for $\mathcal{E} \geq 105\ keV$ because the full-energy injection creates steep, negative energy gradients, which can be seen in the full beam distribution function in Figure 9. A simpler picture of the distribution function is shown in Figure 20, where P_ϕ and μ have been integrated over. These energy gradients reduce ω_* so that $n\omega_* < \omega$ and the wave is damped. For $60 \leq \mathcal{E}(keV) \leq 105$ the energy gradients are gentle, ω_* is large, and the mode is driven. At $\mathcal{E} \approx 60keV$, the half-energy beam injection again produces strong negative energy gradients, damping the TAE. For $\mathcal{E} < 50\ keV$, particles weakly drive the TAE. A similar effect is observed for weaker (but still significant) resonances $v_{\parallel} = v_A/7$ and $v_A/9$, which correspond to resonance numbers $p = 13$ and 12.

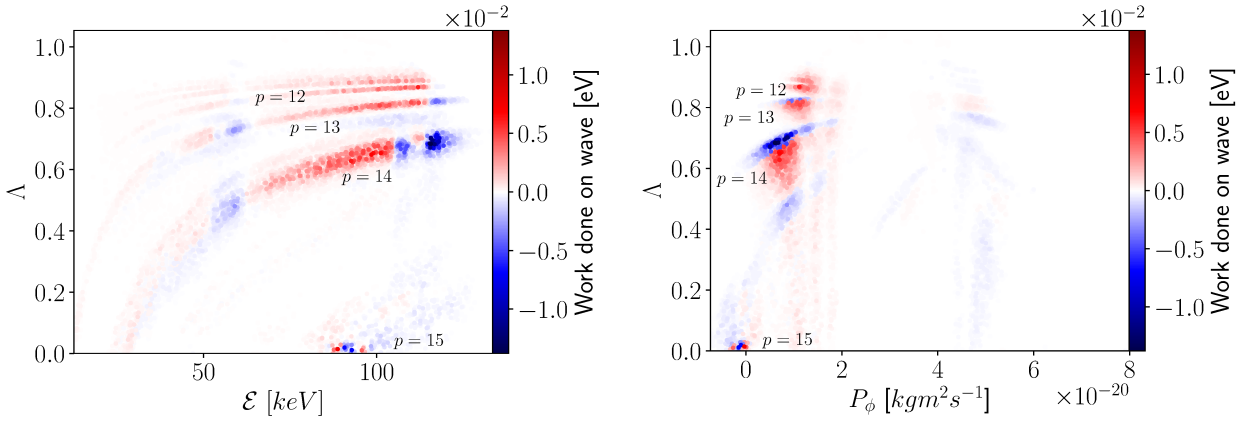

Figure 19: The work done on the $n = 9$ TAE of interest by the highly resonant beam ions in HALO as a function of particle energy $\mathcal{E}$, the pitch invariant $\Lambda = \mu B_0/\mathcal{E}$ and the canonical toroidal angular momentum P_ϕ at time $t = 7.55\ s$ in shot #99503. Red denotes drive and blue denotes damping of the TAE. Key resonances are labelled with their resonance number p.

For TAEs with toroidal mode numbers $n < 8$, the net damping arising from the full energy injection at $\mathcal{E} \geq 105keV$ dominates over drive from $\mathcal{E} < 105keV$. The $v_A/5$ resonance still dominates the mode stability calculation for low n. For TAEs with higher drive than the $n = 9$ mode of interest, the damping contribution from $\mathcal{E} \geq 105keV$ is weaker than the drive from lower energy particles along the $v_A/5$ resonance.

The power transfer is dominated by interactions between particles located at the wave maximum at a major radius $R \approx 3.3\ m$ and the dominant poloidal harmonic $m = -17$, with $m = -16$ also playing a significant role, as shown on the left-hand side of Figure 21. A typical orbit of a resonant ion overlaid over the wave field is shown on the right-hand side of Figure 21. 70% of the net power transfer comes from 0.08% of the particles. Of these highly resonant particles, 3% were trapped particles, 12% were counter-passing and 85% were co-passing ions. Almost all of the resonant counter-passing particles weakly damp the mode, except for weak drive through the $v_A/7$ resonance.

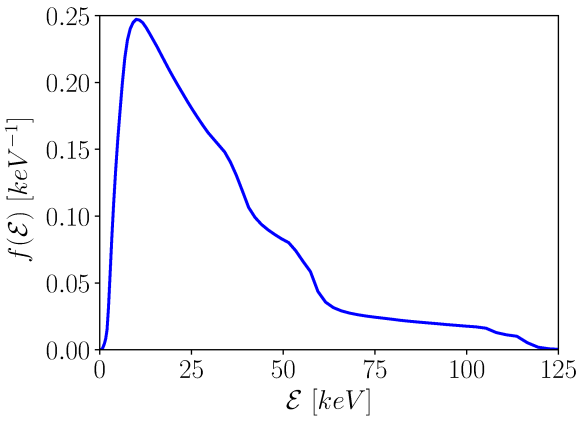

Figure 20: The beam ion energy $\mathcal{E}$ distribution function $f(\mathcal{E})$ integrated over the magnetic moment and canonical toroidal angular momentum at time $t = 7.55\ s$ in shot #99503.

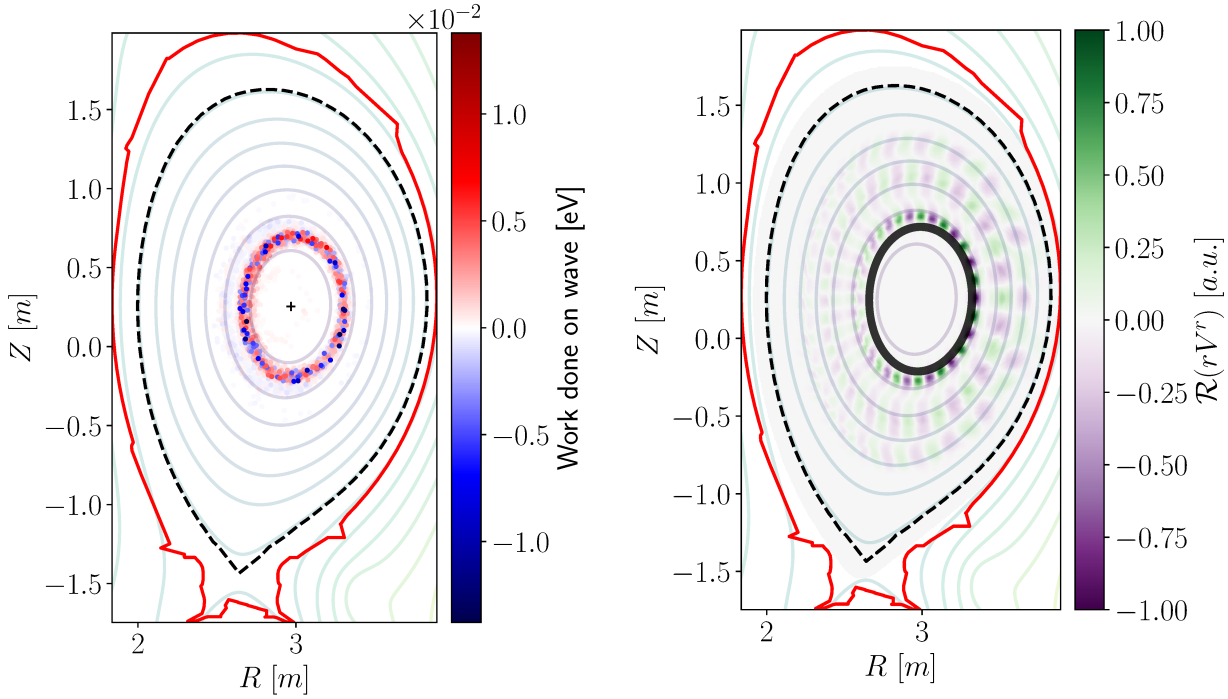

Figure 21: Left: the work done on the net-driven $n = 9$ TAE by highly resonant beam ions in HALO at time $t = 7.55\ s$ in shot #99503 as a function of major radius R and height Z, where red denotes drive and blue denotes damping of the TAE. Right: a typical orbit of a highly resonant ion superimposed on the structure of the wave field. In both figures flux contours are shown in the background, a dashed black line denotes the last closed flux surface and the first wall is shown by a solid red line.

3.7 Power transfer between the $n = 9$ TAE and alpha particles

The power transfer to the $n = 9$ TAE from the population of alpha particles is shown in Figure 22. As for the beam population, the P_ϕ gradients in the alpha particle distribution function drive the TAE. The majority of the mode drive comes from passing particles, with trapped particles contributing just 5

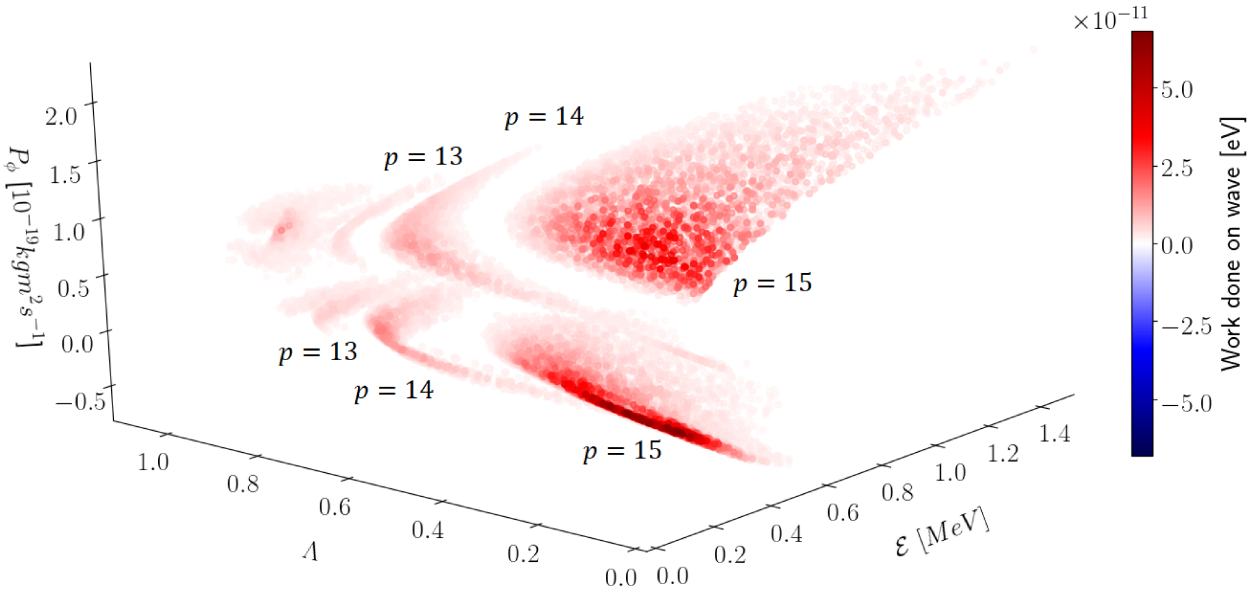

Figure 22: The work done on the $n = 9$ TAE of interest by the highly resonant alpha particles in HALO as a function of particle energy $\mathcal{E}$, the pitch invariant $\Lambda = \mu B_0/\mathcal{E}$ and the canonical toroidal angular momentum P_ϕ at time $t = 7.55\ s$ in shot #99503. Red denotes drive and blue denotes damping of the TAE. Key resonances are labelled with their resonance number p.

% of the net power transfer. Co-passing particles contribute 57 % of the drive, while counter-passing particles contribute 38 %. The drive from co-passing and counter-passing particles can be seen at $P_\phi \lesssim 2.5 \times 10^{-20}\ kgm^2s^{-1}$ and $P_\phi \gtrsim 1.0 \times 10^{-19}\ kgm^2s^{-1}$, respectively. The dominant driving contributions from both the co-passing and counter-passing populations are transferred through the $v_\parallel = v_A/3$ $(p = 15)$ resonance, which is radially extended. There is also a significant contribution to the mode stability from the $v_\parallel = v_A/5$ $(p = 14)$ resonance closer to the trapped-passing boundary. Weak power transfer from $v_\parallel = v_A/7$ and trapped particle resonances (around $\mathcal{E} \approx 500\ keV$) are also visible.

As for beam ions, the power transfer from alpha particles peaks around a major radius $R \approx 3.3\ m$, as shown by the left-hand side of Figure 23. However, both co- and counter-passing alpha particles contribute significant net power transfer to the TAE. Both orbit types are visible on the left-hand side of Figure 23 due to the large orbit width of the resonant alpha particles, which have large $v_\parallel$. Typical orbits of two highly resonant co- and counter-passing alpha particles are shown in the right-hand side of Figure 23. The gyroradii of the highly resonant alpha particles are relatively small because they are deeply passing particles with low $v_\perp$.

4 Conclusions

During steady, low power ($P_{NBI} = 11.6\ MW$) beam injection in our JET D-T experiment, we observed high-frequency modes using two diagnostics, an interferometer and a reflectometer. These modes were observed with weak amplitudes at a frequency $f = 155\ kHz$ and were located at major radii $3.1 \leq R(m) \leq 3.3$ with errorbars of $\pm 0.1\ m$. Using the linear MHD code MISHKA, we identified these modes as TAEs. 21 TAEs with toroidal mode numbers $0 \leq n \leq 12$ fit experimental observations. We

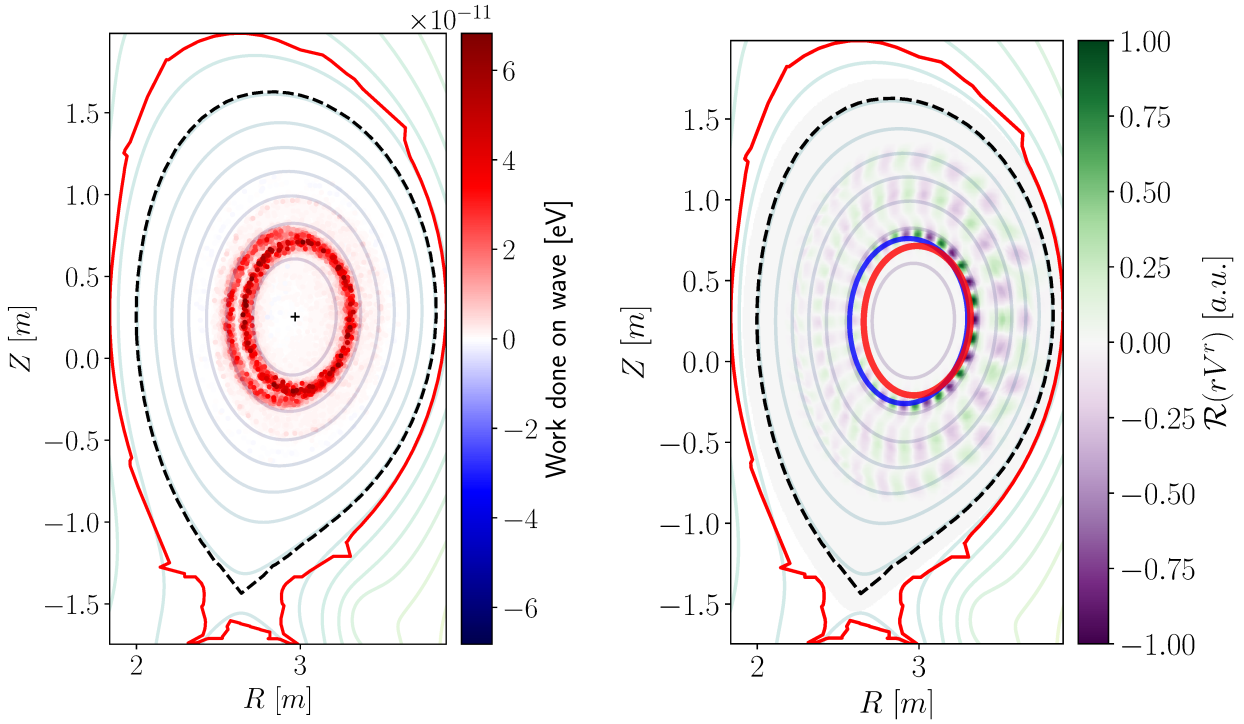

Figure 23: Left: the work done on the net-driven $n = 9$ TAE by highly resonant alpha particles in HALO at time $t = 7.55$ s in shot #99503 as a function of major radius R and height Z, where red denotes drive and blue denotes damping of the TAE. Right: typical orbits of two highly resonant alpha particles superimposed on the structure of the wave field, red shows a co-current orbit and blue denotes a counter-current orbit. In both figures flux contours are shown in the background, a dashed black line denotes the last closed flux surface and the first wall is shown by a solid red line.

modelled beam ions and alpha particles using the full orbit particle tracking code LOCUST. Exploiting the latest GPU hardware to follow $\sim 10^7$ markers allows us to calculate a smooth, high-resolution distribution. The low statistical noise in these distribution functions means it was possible to calculate mode stability without taking analytical fits of the distribution function, which is typically required to remove spurious gradients but removes important features of the distribution function including the trapped-passing boundary, the full, half and third energy beam injection, the magnetic axis boundary and even the $E \geq \mu B$ boundary.

We calculated the stability of the 21 candidate modes using the wave-particle interaction code HALO. These calculations revealed beam ions can drive TAEs with toroidal mode numbers $n \geq 8$, while TAEs with $n < 8$ were damped by the beam ion population. The maximum drive from beam ions is $\gamma_d/\omega \approx 1.0\%$. The surprising discovery that beam ions can drive high n TAEs in JET was supported by a simple analytical calculation of the ion diamagnetic frequency. The drive from alpha particles was also assessed. All but one of the candidate TAEs were weakly driven by alpha particles, with peak growth rates $\gamma_\alpha/\omega \approx 0.05\%$ due to the low alpha power generated in our experiment. Guiding centre calculations were found to significantly overestimate growth rates compared to full orbit calculations for both beam and alpha particles.

Non-ideal damping effects were computed for each candidate mode using the CASTOR code. Radiative damping was found to be dominant, particularly for high m even modes, in agreement with previous calculations on JET [8]. However, collisional damping was significant for even modes at larger radii. Continuum damping was weak for all modes. Ion Landau damping was calculated using a Maxwellian distribution function for thermal ions in HALO, but damping rates were small compared to radiative and collisional damping due to the low plasma temperature and high magnetic field.

Comparing the drive from energetic particles to damping from thermal particles, we found a single net-driven TAE with a net growth rate $\gamma/\omega = 0.02\%$, with the remaining 20 modes net-damped. This TAE matches experimental observations with a frequency $f = 163kHz$ and location $R = 3.31m$. The TAE was driven by co-passing particles due to P_ϕ gradients through the $v_\parallel = v_A/5$ resonance (resonance number $p = 14$). The power transfer from alpha particles to the TAE largely occurs through the $v_\parallel = v_A/3$ resonance. Both co- and counter-passing alpha particles contribute a significant amount of net power transfer. Interactions between fast particles and the mode occur mainly through the poloidal harmonic $m = -17$, with $m = -16$ also playing an important role. The stability of each TAE is largely dictated by the balance between drive and damping from $v_\parallel = v_A/5$ resonance with beam ions. Additional sideband resonances contribute significant drive for both the alpha particle and beam ion populations.

Beam-driven TAEs have not been identified in JET before. The absence of ICRH-accelerated ions in this experiment allows for a more accurate determination of the source of the mode drive. The high magnetic field and low electron temperature in our experiment reduces non-ideal damping effects $\sim k_\perp \rho_i$. Additionally, the drive from beam ions and alpha particles was boosted by a relatively high safety factor profile.

The modelling framework described in this paper substantially enhances previous modelling efforts. Stability calculations using distribution functions that do not require fitting are capable of more accurately predicting the excitation of Alfvén eigenmodes in future burning plasmas, such as those expected in ITER.

Acknowledgements

The authors thank F. Palermo and anonymous reviewers for useful comments that have improved this manuscript. This work has been carried out within the framework of the EUROfusion Consortium, funded by the European Union via the Euratom Research and Training Programme (Grant Agreement No 101052200 — EUROfusion) and from the EPSRC [grant number EP/W006839/1]. Views and opinions expressed are however those of the author(s) only and do not necessarily reflect those of the European Union or the European Commission. Neither the European Union nor the European Commission can be held responsible for them. To obtain further information on the data and models underlying this paper please contact PublicationsManager@ukaea.uk. Author R.A. Tinguely was supported by US DOE Grant DE-SC0014264.

References

[1] C. Z. Cheng, L. Chen, and M. S. Chance. High-n ideal and resistive shear Alfvén waves in tokamaks. *Annals of Physics*, 161(1):21 – 47, 1985.

[2] F. Porcelli, R. Stankiewicz, W. Kerner, and H. L. Berk. Solution of the drift-kinetic equation for global plasma modes and finite particle orbit widths. *Physics of Plasmas*, 1(3):470–480, 1994.

[3] H. L. Berk, W. Horton, M. N. Rosenbluth, and P. H. Rutherford. Microinstability theory of two-energy-component toroidal systems. *Nuclear Fusion*, 15(5):819–844, 1975.

[4] J. A. Rome, D. G. McAlees, J. D. Callen, and R. H. Fowler. Particle-orbit loss regions and their effects on neutral-injection heating in axisymmetric tokamaks. *Nuclear Fusion*, 16(1):55, 1976.

[5] C. Di Troia. Bayesian derivation of plasma equilibrium distribution function for tokamak scenarios and the associated landau collision operator. *Nuclear Fusion*, 55(12):123018, 2015.

[6] M. Fitzgerald, S. E. Sharapov, P. Siren, E. Tholerus, M. Dreval, G. Szepesi, P. Vallejos, T. Johnson, N. Fil, J. Ferreira, P. Rodrigues, A. Figueiredo, D. Borba, R. Coelho, F. Nabais, J. Mailloux, H. J. C. Oliver, C. Di Troia, F. Napoli, Ž. Štancar, R. Dumont, D. Keeling, and JET Contributors. Toroidal Alfvén eigenmode stability in JET internal transport barrier afterglow experiments. *Nuclear Fusion*, 62(10):106001, 2022.

[7] R. J. Akers, E. Verwichte, T. J. Martin, S. D. Pinches, and R. Lake. GPGPU Monte Carlo Calculation of Gyro-Phase Resolved Fast Ion and n-State Resolved Neutral Deuterium Distributions. *39th EPS Conference and 16th Int. Congress on Plasma Physics*, P5.088:3217–3226, 2012.

[8] M. Fitzgerald, J. Buchanan, R. J. Akers, B. N. Breizman, and S. E. Sharapov. HALO: A full-orbit model of nonlinear interaction of fast particles with eigenmodes. *Computer Physics Communications*, 252:106773, 2020.

[9] D. Borba, H. L. Berk, B. N. Breizman, A. Fasoli, F. Nabais, S. D. Pinches, S. E. Sharapov, D. Testa, and contributors to the EFDA-JET Workprogramme. Modelling of Alfvén waves in JET plasmas with the CASTOR-K code*. *Nuclear Fusion*, 42(8):1029, 2002.

[10] R. J. Dumont, J. Mailloux, V. Aslanyan, M. Baruzzo, C. D. Challis, I. Coffey, A. Czarnecka, E. Delabie, J. Eriksson, J. Faustin, J. Ferreira, M. Fitzgerald, J. Garcia, L. Giacomelli, C. Giroud, N. Hawkes, Ph. Jacquet, E. Joffrin, T. Johnson, D. Keeling, D. King, V. Kiptily, B. Lomanowski, E. Lerche, M. Mantsinen, L. Meneses, S. Menmuir, K. McClements, S. Moradi, F. Nabais, M. Nocente, A. Patel, H. Patten, P. Puglia, R. Scannell, S. Sharapov, E. R. Solano, M. Tsalas, P. Vallejos, H. Weisen, and JET contributors. Scenario development for the observation of alpha-driven instabilities in JET DT plasmas. *Nuclear Fusion*, 58(8):082005, 2018.

[11] J. Seo, J. Kim, J. Mailloux, R. J. Dumont, M. Fitzgerald, S. E. Sharapov, D. L. Keeling, F. Koechl, F. J. Casson, C. Y. Lee, T. S. Hahm, Y. S. Na, and JET contributors. Parametric study of linear stability of toroidal Alfvén eigenmode in JET and KSTAR. *Nuclear Fusion*, 60(6):066008, 2020.

[12] S. E. Sharapov, H. J. C. Oliver, J. Garcia, D. L. Keeling, M. Dreval, V. Goloborod'ko, Ye. O. Kazakov, V. G. Kiptily, Ž. Štancar, P. J. Bonofiglo, R. Coelho, J. Ferreira, A. Figueiredo, N. Fil, M. Fitzgerald, F. Nabais, M. Nocente, P. G. Puglia, J. Rivero-Rodriguez, P. Rodrigues, M. Salewski, R. A. Tinguely, L. E. Zakharov, , and JET contributors. Experiments on excitation of Alfvén eigenmodes by alpha-particles with bump-on tail distribution in JET DTE2 plasmas. *submitted to Nuclear Fusion D-T special issue*, 2023.

[13] A. Boboc, L. Zabeo, and A. Murari. Simultaneous cotton-mouton and faraday rotation angle measurements on jet. *Review of Scientific Instruments*, 77(10):10F324, 2006.

[14] S. Hacquin, S. E. Sharapov, B. Alper, C. D. Challis, A. Fonseca, E. Mazzucato, A. Meigs, L. Meneses, I. Nunes, S. D. Pinches, and the JET EFDA Contributors. Localized X-mode reflectometry measurements of Alfvén eigenmodes on the JET tokamak. *Plasma Physics and Controlled Fusion*, 49(9):1371, 2007.

[15] M. Dreval, S. E. Sharapov, Ye. O. Kazakov, J. Ongena, M. Nocente, R. Calado, R. Coelho, J. Ferreira, A. Figueiredo, M. Fitzgerald, J. Garcia, C. Giroud, N. C. Hawkes, V. G. Kiptily, F. Nabais, M. F. F. Nave, H. Weisen, T. Craciunescu, M. Salewski, Ž. Štancar, and JET Contributors. Alfvén cascade eigenmodes above the TAE-frequency and localization of Alfvén modes in D–3He plasmas on JET. *Nuclear Fusion*, 62(5):056001, 2022.

[16] L. L. Lao, H. St. John, R. D. Stambaugh, A. G. Kellman, and W. Pfeiffer. Reconstruction of current profile parameters and plasma shapes in tokamaks. *Nuclear Fusion*, 25(11):1611, 1985.

[17] M. Baruzzo, B. Alper, T. Bolzonella, M. Brix, P. Buratti, C. D. Challis, F. Crisanti, E. de la Luna, P. C. de Vries, C. Giroud, N. C. Hawkes, D. F. Howell, F. Imbeaux, E. Joffrin, H. R. Koslowski, X. Litaudon, J. Mailloux, A. C. C. Sips, O. Tudisco, and JET-EFDA contributors. Neoclassical tearing mode (NTM) magnetic spectrum and magnetic coupling in JET tokamak. *Plasma Physics and Controlled Fusion*, 52(7):075001, 2010.

[18] R. J. Hawryluk. An empirical approach to tokamak transport. In B. Coppi, G. G. Leotta, D. Pfirsch, R. Pozzoli, and E. Sindoni, editors, *Physics of Plasmas Close to Thermonuclear Conditions*, pages 19–46. Pergamon, 1981.

[19] G. T. A. Huysmans, J. P. Goedbloed, and W. Kerner. Isoparametric Bicubic Hermite Elements for Solution of the Grad-Shafranov Equation. *International Journal of Modern Physics C*, 02(01):371–376, 1991.

[20] G. T. A. Huysmans, S. E. Sharapov, A. B. Mikhailovskii, and W. Kerner. Modeling of diamagnetic stabilization of ideal magnetohydrodynamic instabilities associated with the transport barrier. *Physics of Plasmas*, 8(10):4292–4305, 2001.

[21] A. B. Mikhailovskii, G. T. A. Huysmans, W. O. K. Kerner, and S. E.. Sharapov. Optimization of computational MHD normal-mode analysis for tokamaks. *Plasma Phys. Rep.*, 23:844–857, 1997.

[22] S. H. Ward, R. Akers, A. S. Jacobsen, P. Ollus, S. D. Pinches, E. Tholerus, R. G. L. Vann, and M. A. Van Zeeland. Verification and validation of the high-performance Lorentz-orbit code for use in stellarators and tokamaks (LOCUST). *Nuclear Fusion*, 61(8):086029, 2021.

[23] A. Pankin, D. McCune, R. Andre, G. Bateman, and A. Kritz. The tokamak Monte Carlo fast ion module NUBEAM in the National Transport Code Collaboration library. *Computer Physics Communications*, 159(3):157–184, 2004.

[24] E. Hirvijoki, O. Asunta, T. Koskela, T. Kurki-Suonio, J. Miettunen, S. Sipilä, A. Snicker, and S. Äkäslompolo. Ascot: Solving the kinetic equation of minority particle species in tokamak plasmas. *Computer Physics Communications*, 185(4):1310–1321, 2014.

[25] H. S. Bosch and G. M. Hale. Improved formulas for fusion cross-sections and thermal reactivities. *Nuclear Fusion*, 32(4):611, 1992.

[26] W. W. Heidbrink. Analytical expressions for fusion spectra produced in "beam - target" fusion reactions. *Review of Scientific Instruments*, 56(5):1098–1099, 1985.

[27] R. E. Denton and M. Kotschenreuther. δf algorithm. *Journal of Computational Physics*, 119(2):283–294, 1995.

[28] T. Fülöp, M. Lisak, Ya. I. Kolesnichenko, and D. Anderson. Finite orbit width stabilizing effect on toroidal Alfvén eigenmodes excited by passing and trapped energetic ions. *Plasma Physics and Controlled Fusion*, 38(6):811, 1996.

[29] R. R. Mett and S. M. Mahajan. Kinetic theory of toroidicity-induced Alfvén eigenmodes. *Physics of Fluids B: Plasma Physics (1989-1993)*, 4(9):2885–2893, 1992.

[30] J. W. Connor, R. O. Dendy, R. J. Hastie, D. Borba, G. Huysmans, W. Kener, and S. Sharapov. Non-ideal Effects on Toroidal Alfvén Eigenmode Stability. In Geneva EPS, editor, *Proceed. of 21st EPS Conference*, volume **18B**, page 616, 1994.

[31] P. Rodrigues, A. Figueiredo, J. Ferreira, R. Coelho, F. Nabais, D. Borba, N. F. Loureiro, H. J. C. Oliver, and S. E. Sharapov. Systematic linear-stability assessment of Alfvén eigenmodes in the presence of fusion α-particles for ITER-like equilibria. *Nuclear Fusion*, 55(8):083003, 2015.

[32] A. C. A. Figueiredo, P. Rodrigues, D. Borba, R. Coelho, L. Fazendeiro, J. Ferreira, N. F. Loureiro, F. Nabais, S. D. Pinches, A. R. Polevoi, and S. E. Sharapov. Comprehensive evaluation of the linear stability of Alfvén eigenmodes driven by alpha particles in an ITER baseline scenario. *Nuclear Fusion*, 56(7):076007, 2016.

[33] N. N. Gorelenkov and S. E. Sharapov. On the collisional damping of TAE-modes on trapped electrons in tokamaks. *Physica Scripta*, 45(2):163, 1992.

[34] F. Nabais, V. Aslanyan, D. Borba, R. Coelho, R. Dumont, J. Ferreira, A. Figueiredo, M. Fitzgerald, E. Lerche, J. Mailloux, M. Mantsinen, P. Rodrigues, M. Porkolab, P. Puglia, S. E. Sharapov, and JET Contributors. TAE stability calculations compared to TAE antenna results in JET. *Nuclear Fusion*, 58(8):082007, 2018.

[35] A. Hasegawa and L. Chen. Kinetic processes in plasma heating by resonant mode conversion of Alfvén wave. *Physics of Fluids (1958-1988)*, 19(12):1924–1934, 1976.

[36] G. W. Bowden, A. Könies, M. J. Hole, N. N. Gorelenkov, and G. R. Dennis. Comparison of methods for numerical calculation of continuum damping. *Physics of Plasmas*, 21(5):052508, 2014.

[37] B. Orwiler. *Oscilloscope Vertical Amplifiers*. Tektronix, Inc., Beaverton, OR, 1969.

A Do we need a detailed distribution function?

Finally, it is prudent to check whether it is necessary to use a detailed beam distribution for stability calculations, or whether a simplified distribution function closer to the slowing down distribution function is sufficient to obtain an accurate growth rate. The distribution function is simplified by smoothing it with a multidimensional Gaussian filter [37], which is routinely used to denoise or blur images. The distribution function becomes more smooth as the standard deviation of the Gaussian kernel σ increases, as shown in Figure 24. When σ is large enough to flatten the distribution function to the boundary in invariant coordinates, the distribution function is reflected from the boundary.

A Gaussian filter with standard deviation $\sigma = 1$ produces a distribution function where most of the detail is retained — the trapped-passing boundary and the full, half and third energy beam injection are still visible. $\sigma = 5$ produces a distribution function where only the approximate shape of the original is retained, with all internal structure smoothed over and gradients eroded. The distinction between the full, half and third energy injection is no longer clear. The distribution function produced with $\sigma = 20$ is unrecognisable compared to the original distribution function but is similar to a slowing down distribution fit. The 1D density and pressure profiles flatten with the distribution function as σ increases.

The standard deviation of the Gaussian filter is scanned and HALO is used to calculate the growth rate for each distribution function, with the resultant growth rates shown in Figure 25. For small standard

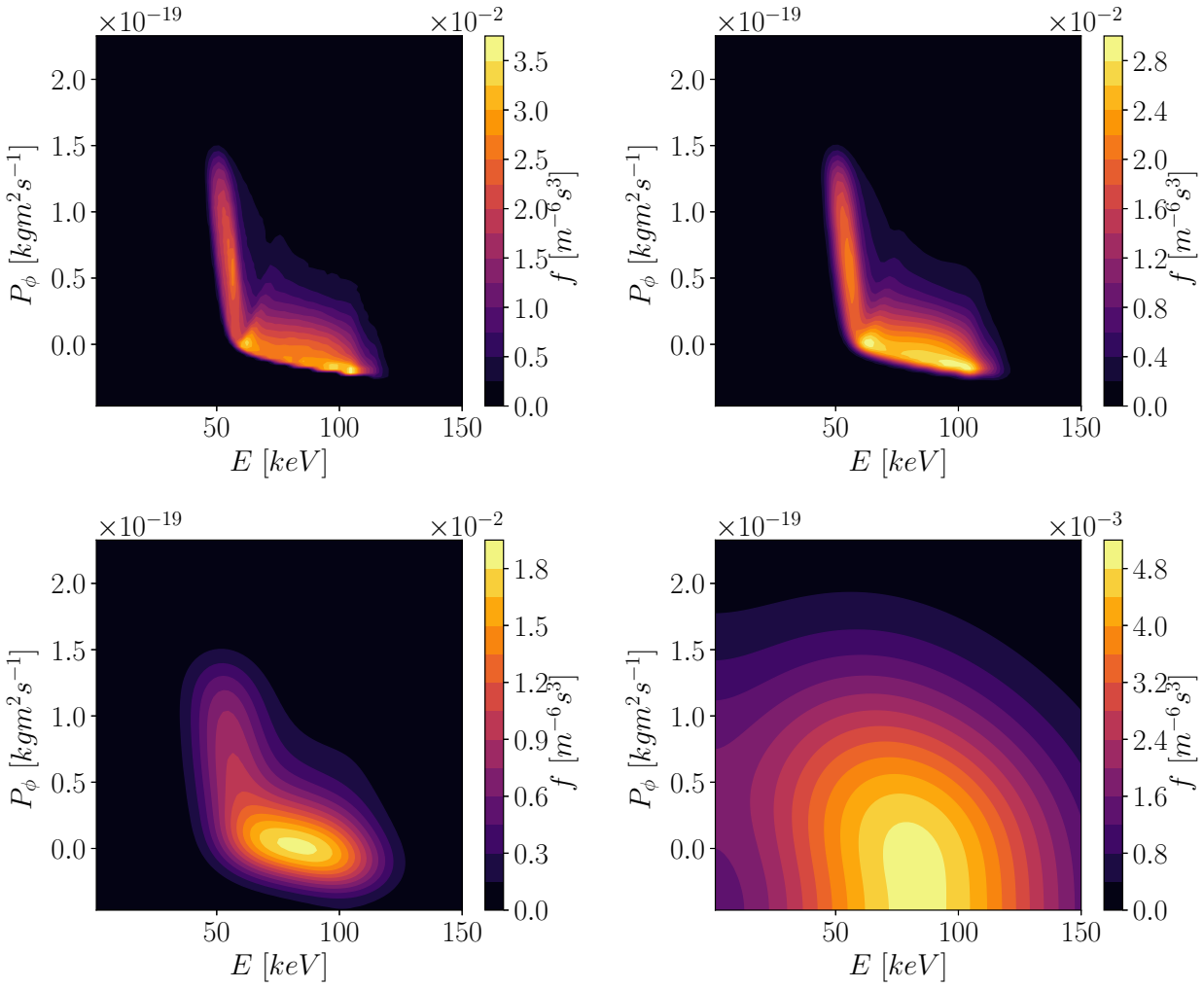

Figure 24: The co-current beam distribution function f as a function of energy E and toroidal canonical angular momentum P_ϕ for magnetic moment $\mu = 15.2keV/T$ and standard deviation of the Gaussian filter: $\sigma = 0.0$ (top left), $\sigma = 1.0$ (top right), $\sigma = 5.0$ (bottom left), and $\sigma = 20.0$ (bottom right) at time $t = 7.55\ s$ in shot #99503.

deviations $\sigma \leq 1$, the growth rate does not change significantly. However, for $\sigma > 1$, the growth rate begins to decrease rapidly with σ because P_ϕ gradients are reduced by the smoothing process. Standard deviations $\sigma > 4.5$ produce distribution functions that yield damping of the TAE because the power transfer.

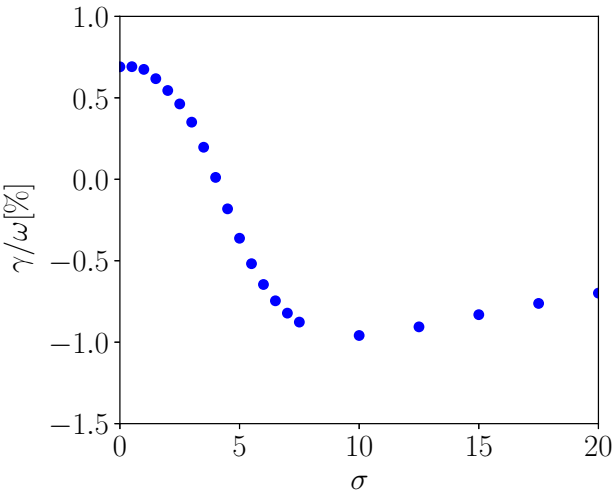

Figure 25: The linear growth rate of the $n = 9$ TAE of interest at time $t = 7.55\ s$ in shot #99503 as a function of the Gaussian filter standard deviation σ used to smooth the beam distribution function.